**Proceedings of the ASME 2024**
**Aerospace Structures, Structural Dynamics, and Materials Conference**
**SSDM2024**
**April 29 - May 1, 2024, Renton, Washington**

**SSDM2024-121620**



# STRUCTURAL AND AERODYNAMIC CHARACTERISTICS OF MICRO-PERFORATED POROUS SHEETS FOR LAMINAR FLOW CONTROL

**Hendrik Traub*, Jan Kube, Siby Jose, Adarsh Prasannakumar, Christian Hühne**

Technische Universität Braunschweig, Braunschweig, Germany

## ABSTRACT

*Laminar flow control shows an unparalleled potential to increase the energy efficiency of state-of-the-art transport aircraft. However, active boundary layer suction requires micro-metre precision and is associated with extensive manufacturing effort. This study investigates new manufacturing technologies, such as additive manufacturing and laminating of porous sheets for boundary layer suction. The new porous sheets extend the design space of porous skins for laminar flow control and aim to reduce their manufacturing effort. This research shows the feasibility of additively manufactured and laminated porous sheets with perforation diameters below* 250 µm *and pressure drop characteristics comparable to available etched and laser-drilled sheets.*

**Keywords: HLFC, LFC, AM, Preist, Perforation, Porous**

## 1. MICRO-PERFORATED SHEETS FOR LAMINAR FLOW CONTROL

Compared to state-of-the-art transport aircraft, aircraft designed for laminar boundary layer flow promise a significant performance increase by decreasing the aircraft's viscous drag by up to 90 % [1]. To achieve laminar boundary layer flow, current research focuses on passive flow control, such as natural laminar flow (NLF) and active flow control, such as laminar flow control (LFC). NLF achieves transition delay with an aerofoil design providing a favourable pressure gradient to dampen the growth of Tollmien-Schlichting instabilities in combination with high surface quality. LFC achieves transition delay with active boundary layer suction [2]. While NLF only results in a partial laminarisation of transport aircraft, LFC has the potential of a fully laminar aircraft [3] but requires active systems for boundary layer suction [4]. Combinations of NLF and LFC promise a high degree of laminar boundary layer with reduced manufacturing and systems effort. They are commonly investigated as hybrid laminar flow control (HLFC) [5]. Therefore, boundary layer suction as a part of HLFC is a promising approach to lower the operating costs and the carbon footprint of state-of-the-art transport aircraft.

*Corresponding author: h.traub@tu-braunschweig.de

The structural components enabling boundary layer suction are micro-perforated sheets. In recent developments, perforated sheets used as aircraft skins are thin, etched foils [6] or thicker laser-drilled sheets [7]. Several laser drilling processes, single-pulse, laser trepanning and laser percussion drilling, were used in the past for drilling micro-perforations of reasonable accuracy [8, 9]. Messaoudia et al. [8] worked on improving the inner surface quality and increasing the diameter of the holes using chemical pickling. However, the post-processing may result in various manufacturing imperfections and thereby change the specified geometrical parameters. Laser-drilled carbon-fibre-reinforced plastics were investigated but not further used for LFC applications because they showed severe structural failure caused by fibre fragmentation resulting from the drilling process [10].

While thin foils are susceptible to stability issues, metallic sheets add significant weight to the wing [11]. Both types are metal-based perforated sheets attracting loads when integrated into the wing structure due to their high Young's modulus. Therefore, this study includes engineering plastics for manufacturing micro-perforated sheets, avoiding significant loading of the suction structure.

Such engineering plastics can be additively manufactured (AM) featuring inherent porosities. AM of micro-perforated sheets enables new suction panel concepts, where whole panels are manufactured as integral parts, avoiding hole blockage and residual stresses resulting from joining. Manufacturing the panel in its final shape allows for three-dimensional curved surfaces.

Next to AM perforated sheets, this study includes carbon-fibre-reinforced plastics (CFRP) laminated on a needle bed tooling, avoiding the destruction of fibres through laser drilling and a laser-drilled polycarbonate (PC) specimen. While the etched and laser-drilled foils and sheets investigated in this study are available on an industrial level [12], the porous CFRP sheets and the AM sheets are produced within the scope of this research.

This study investigates porous sheet specimens' porosity, hole geometry, and perforation quality. To determine the porosity and hole quality of the specimens, an algorithm is developed in this study to detect porosities based on microscopic images

and to return a statistical analysis of hole size, geometry, and their deviations. The combined data of perforation size, quality and geometry allows a direct comparison of industrial available perforated sheets to the AM porous sheets.

The pressure drop, depending on the suction rate, is experimentally determined for all specimens to connect the structural characteristics to the aerodynamic characteristics. In the experiments, the specimens are mounted into a flow bench, where the pressure is measured above and below the specimens. Combined with the measured volume flow, the experiments return a relationship between pressure drop and flow rate for each specimen. This relationship can then be used to fit a physical pressure drop prediction model to the data to understand the aerodynamic characteristics of the different types of micro-perforated porous sheets and their dependence on their geometric characteristics.

The laser-drilling of metal sheets results in a truncated-cone hole geometry, with a larger plenum side diameter (entrance of laser) and a smaller flow side diameter (exit of laser) [10]. Poll et al. [13] experimentally investigate the pressure drop characteristics of laser-drilled micro-perforated titanium sheets with flow-side diameters ranging from 30 µm to 178 µm to fit a modified Goldstein pressure-loss model [14]. Their work addresses the hole tapering by introducing the diameter-dependent modifier K, defined as the ratio of the perforation's flow-side diameter to the plenum-side diameter. However, they concluded this ratio to be too crude to model the pressure drop characteristics of the micro-perforated sheet.

Preist and Paluch [15] developed a statistical approach for assessing HLFC panels regarding their surface imperfections and geometrical variations of the perforation. High-resolution optical microscope measurements were used to study the influence of geometrical imperfections on pressure characteristics. The calculation of diameter depends on image processing and hole contour detection techniques. Two major factors influencing the hole image processing were estimated: magnification and threshold level. For a greyscale image with 256 levels, it was found that a threshold of 35-45 estimates the hole diameter with a 3 % deviation. Based on these optical statistical estimations, a new model was proposed in their work, which considers the conicity of the laser-drilled hole geometry in contrast to the cylindrical hole model proposed by Poll et al. [13].

Bohning and Doerffer [16] developed a transpiration model for pressure loss through micro-perforated sheets. The Bohning-Doerffer (B-D) model relates the normalised pressure drop to the Mach number inside the hole. However, this empirical model depends on experimental measurements of micro-perforated sheets and the calculation of a modified porosity of the sheets named the "aerodynamic porosity". The aerodynamic porosity is not identical to the geometrical porosity of the perforated sheet but rather a coefficient to represent the pressure characteristics. Therefore, the model does not accurately represent the influence of actual perforation size or manufacturing irregularities.

Gibson [17] modelled the flow through a perforated sheet, including both compressibility and frictional effects, hence not assuming a fully developed flow. The model was based on Fanno analysis for a constant-area pipe. Therefore, it is unsuitable for irregular hole shapes produced by different manufacturing processes. For applying HLFC for subsonic aircraft and considering low suction velocities, incompressible flow through the holes can be assumed. In this case, the Preist model [15] captures the required physics and offers a method to include the perforation irregularities in the model. Therefore, the authors of this study chose the Preist model to compare the pressure characteristics of different experimentally investigated micro-perforated porous sheets.

Next to the porosity, perforation diameter and pattern, the surface roughness of the perforated sheets significantly impacts the flow's laminarity. This includes 2D and 3D surface roughness as well as waviness. Distributed roughness can cause earlier transition if the roughness height is above a critical limit [18, 19]. However, the classical roughness parameters such as $R_a$ and $R_t$ are inadequate for HLFC applications [20]. An alternative is the critical Reynolds number ($Re_k$) depending on the local velocity, the kinematic viscosity and the roughness height. Anderson et. Al. proposed a stability criterion where $Re_k$ should be between 100 and 1600 [21]. To identify the roughness height of the different micro-perforated porous sheet types, this study measures the roughness of the surface surrounding the holes.

A comprehensive characterisation of micro-perforated porous sheets requires knowledge of their geometrical and aerodynamic properties. The following sections, therefore, describe the test specimens' manufacturing, microscopic porosity and perforation geometry investigations, surface roughness measurements using a profilometer and aerodynamic pressure drop investigations. These methods result in porosity and pressure drop characteristics for each micro-perforated sheet type. The identified geometric characteristics in terms of porosity and hole geometry further allow the prediction of the pressure drop using the Preist model. A validation of this model is possible by comparing it to the experimentally determined pressure drop characteristics, expanding the model to rectangular and significantly tapered holes. Such a validated model is a prerequisite for designing LFC suction panels, as suggested in [5].

## 2. MANUFACTURING, TESTING AND EVALUATION

This section describes the test matrix of investigated micro-perforated specimens, their manufacturing and the methods used for their geometrical and aerodynamic characterisation. While laser-drilled and etched perforated sheets used for the specimens are purchased for this study, the manufacturing process of AM porous sheets and laminated porous CFRP sheets is part of this study. All specimens are investigated for their perforation geometry and porosity using microscopic images evaluated with a Python-based porosity detection algorithm. The same specimens are then tested for their aerodynamic pressure drop characteristics. In combination with surface roughness measurements, the pressure drop characteristics allow to assess the applicability of the new porous sheet types for LFC applications.

### 2.1 Test specimens and manufacturing

This research compares six different types of perforated and porous sheets. All specimens are circular plates with an outer diameter of $d_o$ = 89.5 mm and designed with a hexagonal perforation pattern. Those specimens not cut from larger perforated

sheets additionally have a restricted perforated area with an inner diameter of $d_i$ = 80.0 mm as shown in Figure 1, to avoid side flow at the sealing area of the flow bench.

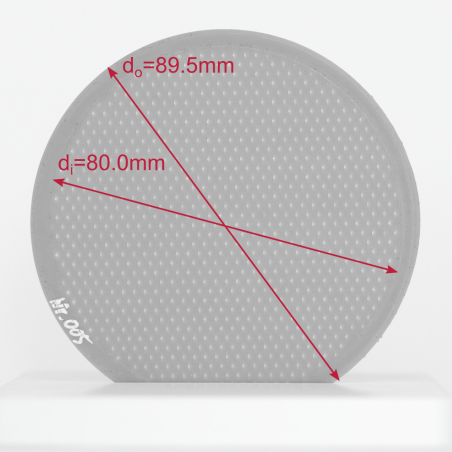


**FIGURE 1: SLA PRINTED POROUS SHEET SPECIMEN NO. 05 WITH A TRUNCATED PYRAMID PERFORATION FOR POROSITY AND PRESSURE DROP INVESTIGATIONS.**

The study includes three sets of industrially manufactured skin types. The baseline specimens are stainless steel (SS) specimens featuring laser-drilled perforations with design diameters of 60 µm, 120 µm and 240 µm and a design porosity of 0.91 % provided by the Institute of Fluid Mechanics of the TU Braunschweig [22]. These specimens are cut from larger sheets initially ordered for the ALTTA project [23] and have a thickness of 0.8 mm. Additional specimens were cut from 0.05 mm thick SS foils with etched perforations. The perforations have a design diameter of 63 µm and a design porosity of 0.91 %. The foils provided by DLR Stuttgart were initially manufactured by Micro-Metal [24] as the outer layer of the TSSD concept [6]. A significant addition to our sample collection was made through the procurement of a laser-drilled polycarbonate (PC) specimen with a hole diameter of 200 µm and a nominal porosity of 0.91 % from Photonicfab [25].

The industrially manufactured specimen set is expanded in this study by AM SS specimens, AM epoxy-resin specimens and laminated CFRP specimens. The porous SS specimens were manufactured using selective laser melting (SLM) with hole diameters of 60 µm, 120 µm and 240 µm and a design porosity of 0.91 %. The epoxy-resin specimens were manufactured using a Stereolithography (SLA) process with quadratic 250 µm by 250 µm perforations and a design porosity of 1.0 %. The laminated CFRP specimens feature a hole diameter of 180 µm and a design porosity of 2.15 %. Table 1 summarises all specimens used in this study.

AM of porous sheets with an equivalent perforation diameter $\leq$ 250 µm and a porosity of $\approx$ 1 % is challenging and has not yet been shown. Preliminary investigations with fused-deposition modelling (FDM), SLA, SLM, Objet and Polyjet printers show that SLA and SLM technologies are promising for printing microperforations [5]. While SLM printers produce metallic parts with rough surfaces, SLA printers produce plastic parts with high surface quality. In this study, SLA-printed and SLM-printed porous specimens are manufactured to quantify the minimum achievable equivalent perforation diameter and the associated pressure drop characteristic.

Perforated sheets for LFC, such as laser-drilled or etched SS sheets, are designed with cylindrical perforation geometries. However, in reality, etched foils show oblique cylinders, while laser-drilled sheets show truncated cones. Figure 2 shows the design hole geometry a), the resulting oblique cylinder from etching b), and the resulting truncated cone from laser-drilling c). This example illustrates the dependence of the hole geometry on the manufacturing process. Preliminary investigations show that in AM, cylinders and truncated cones with only a small slant angle tend to get clogged from support material or resin drawn in by the capillary effect. Therefore, this study focuses on quadratic truncated cones, shown in 2 d).

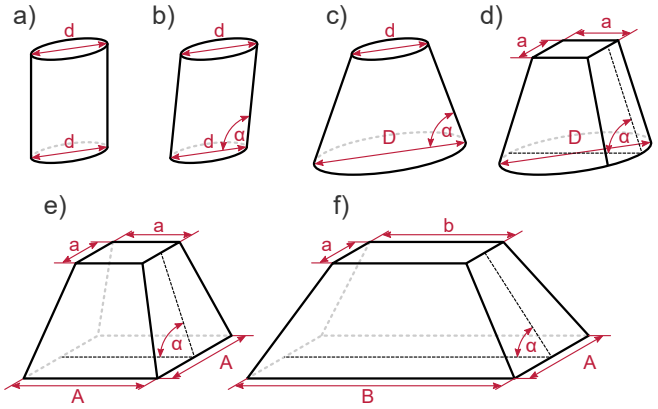


**FIGURE 2: PERFORATION GEOMETRIES INVESTIGATED FOR AM USING SLA: A) CYLINDER; B) OBLIQUE CYLINDER; C) TRUNCATED-CONE; D) QUADRATIC-TRUNCATED-CONE; E) TRUNCATED PYRAMID; F) TRUNCATED PYRAMID SLOT**

The perforation geometries d)-f) in Figure 2 have multiple advantages in AM. The quadratic hole shape reduces the negative impact of the staircase effect on the hole geometry on the suction surface. A large slant angle reduces the tendency of clogged holes by resin or powder in SLA and SLM printing. At the same time, the slant angle reduces the need for supporting the hole walls or reduces the negative effects of unsupported walls, especially when choosing a beneficial printing direction. Therefore, quadratic truncated cones D), truncated pyramids e) and truncated pyramid slots f) are promising geometries for AM.

This study focuses on specimens with quadratic truncated cone perforations (d) for SLA printing. Figure 3 shows this geometry, which is next to truncated pyramid slots (f), the most promising perforation geometry for AM on SLA machines. Even though quadratic-truncated-cone perforations are also a promising geometry for SLM printed specimens, due to their high manufacturing costs, SLM printed specimens are so far limited to cylinders, which require a laser cleaning of the surface to remove hole clogging. Only this post-treatment allows the AM of cylindrical holes.

Next to AM porous sheets, this study introduces laminated porous CFRP sheets with integrated perforations. A needle bed

**TABLE 1: OVERVIEW OF INVESTIGATED POROUS SHEET SPECIMENS.**

| No. | manufacturing | material | nominal thickness in mm | design hole size in mm | design pitch in mm | design porosity in % | perforation geometry | surface treatment |
|---|---|---|---|---|---|---|---|---|
| 07 | vacuum bag | CFRP | 0.68 | 0.180 | 1.17 | 2.15 | cylinder (a) | none |
| 08 | etched | SS | 0.05 | 0.063 | 0.63 | 0.91 | oblique cylinder (b) | polished |
| 09 | etched | SS | 0.05 | 0.063 | 0.63 | 0.91 | oblique cylinder (b) | polished |
| 10 | etched | SS | 0.05 | 0.063 | 0.63 | 0.91 | oblique cylinder (b) | polished |
| 11 | laser drilled | SS | 0.80 | 0.060 | 0.60 | 0.91 | truncated-cone (c) | polished |
| 12 | laser drilled | SS | 0.80 | 0.120 | 1.20 | 0.91 | truncated-cone (c) | polished |
| 13 | laser drilled | SS | 0.80 | 0.240 | 2.40 | 0.91 | truncated-cone (c) | polished |
| 14 | SLM | SS | 0.8 | 0.240 | 2.40 | 0.91 | cylinder (a) | laser cleaned |
| 15 | SLM | SS | 0.8 | 0.240 | 2.40 | 0.91 | cylinder (a) | laser cleaned |
| 16 | SLM | SS | 0.8 | 0.120 | 1.20 | 0.91 | cylinder (a) | laser cleaned |
| 17 | SLM | SS | 0.8 | 0.120 | 1.20 | 0.91 | cylinder (a) | laser cleaned |
| 18 | SLM | SS | 0.8 | 0.060 | 0.60 | 0.91 | cylinder (a) | laser cleaned |
| 19 | SLA | Grey | 0.8 | 0.250x0.250 | 2.686 | 1.00 | quadratic-truncated-cone (d) | none |
| 20 | SLA | Grey | 0.8 | 0.250x0.250 | 2.686 | 1.00 | quadratic-truncated-cone (d) | none |
| 21 | SLA | Grey | 0.8 | 0.250x0.250 | 2.686 | 1.00 | quadratic-truncated-cone (d) | none |
| 25 | laser drilled | PC | 0.8 | 200 | 2.0 | 0.91 | truncated-cone (c) | none |

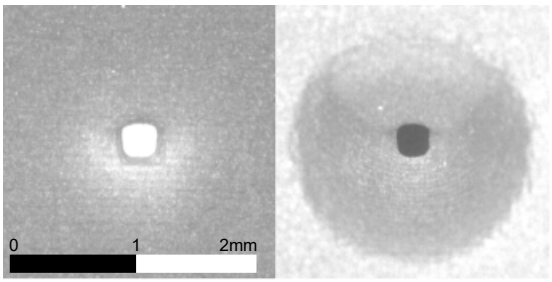


**FIGURE 3: MICROSCOPIC IMAGE OF THE UPPER (LEFT) AND LOWER (RIGHT) SIDE OF THE QUADRATIC-TRUNCATED-CONE PRINTED WITH SLA.**

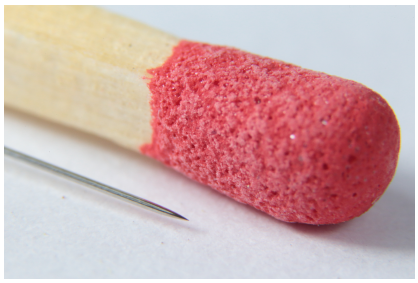

**FIGURE 4: SINGLE ACUPUNCTURE NEEDLE WITH A DIAMETER OF 180 $\mu$m USED FOR MANUFACTURING THE NEEDLE-BED TOOLING. THE NEEDLES ARE COATED WITH MEDICAL SILICONE, FUNCTIONING AS A RELEASE FILM.**

tool is used in the CFRP manufacturing setup to integrate the perforations without cutting the fibres or removing the protective resin film around the fibres. The needles have a diameter of 0.18 mm and a handle diameter of 1.17 mm [26]. Figure 4 shows the conical shape of the needle tip with a standard match as a size reference. The needle handle diameter determines the distance of the needles, arranged in a hexagonal pattern, resulting in a design porosity of 2.15 %. Figure 5 shows the needle bed tool with its 1848 needles resulting in 49.14 mm by 48.03 mm perforation area.

The CFRP specimen is designed as a thin porous sheet of two woven ±45° carbon fibre layers. Figure 6 shows the manufacturing layout, where the porous CFRP specimen is cured below the needle bed tool using a resin injection moulding process. A cork sheet below the fibre material allows the needles to penetrate through the specimen. The resulting specimen has a total thickness of 0.68 mm and a porous area of 49.14 mm by 48.03 mm, which does not cover the full specimen area.

**FIGURE 5: NEEDLE-BED TOOLING FOR MANUFACTURING CFRP SHEETS WITH INTEGRATED POROSITIES.**

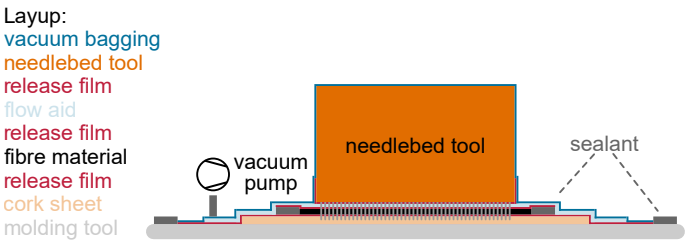


**FIGURE 6: MANUFACTURING LAYUP OF THE CFRP SPECIMEN.**

### 2.2 Porosity evaluation

The perforation characterisation in this study includes the determination of perforation geometries, their pitch and pattern, and the porosity of the specimens. The basis of the characterisation are images taken at high resolution with background light on a Zeiss Smartzoom 5 microscope [27]. A Python-based porosity detection algorithm allows detecting the contours of the holes using the OpenCV library [28]. The mean equivalent diameter calculated from the perforation area in combination with the mean pitch allows the determination of the specimens' porosity.

A rendered CAD image of specimen No. 19 is used to determine the accuracy of the porosity detection tool. Figure 7 shows a section of the rendered image, including the contours of the detected holes. With an equivalent detected edge length of 250.8 µm the deviation from the design edge length of 250 µm is 0.31 %. Using a design pitch of 2.5 mm results in a design porosity $\Phi$ of 1.155 % according to equation (2). With a detected mean pitch of $p = 2.5240$ mm, the detected porosity is evaluated to be 1.1664 %. The resulting porosity deviation below 1 % shows the high accuracy of the image-based, automated porosity detection algorithm.

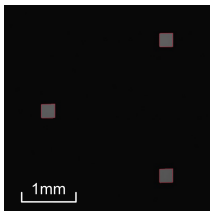


**FIGURE 7: CONTOURS DETECTED BY THE IMAGE PROCESSING SOFTWARE FOR A RENDERED IMAGE OF SPECIMEN NO. 19.**

$$\Phi_{circ} = \frac{\pi d^2}{4A} = \frac{\pi d^2}{2\sqrt{3}p^2} \tag{1}$$

$$\Phi_{square} = \frac{a^2}{A} = \frac{2a^2}{\sqrt{3}p^2} = \frac{2 \cdot 0.25^2}{\sqrt{3} \cdot 2.5^2} = 1.155 \tag{2}$$

The detected porosity significantly depends on the value threshold of the hue-saturation-value (HSV) colourspace used in the filtering function inRange of the OpenCV library. Figure 8 shows the change in detected porosity depending on the lower threshold value. The lower the threshold value, the darker the detected porosity. The whole image is detected as one large porosity when the threshold is zero. For high threshold values, the detected porosity area vanishes. The porosity between these extremes can be modelled with high accuracy as a cubic spline, where the infliction point determines the value threshold leading to the maximum value gradient. In this study, the optimum value threshold is determined by the cubic spline regression for each specimen.

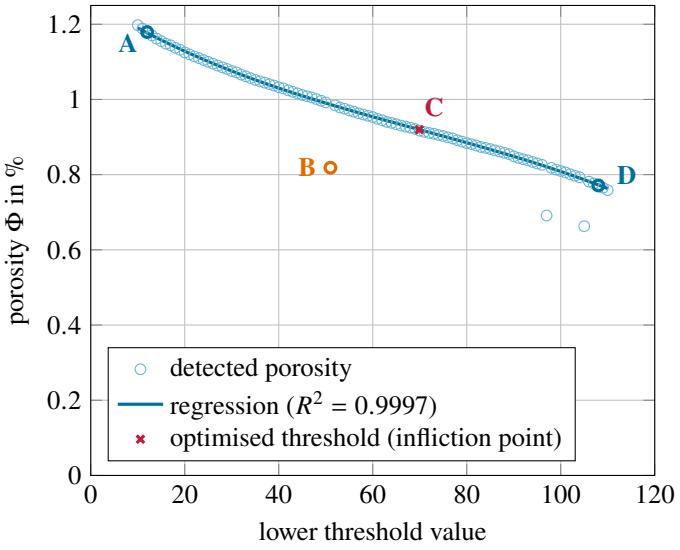


**FIGURE 8: THE DETECTED POROSITY DEPENDS ON THE LOWER VALUE THRESHOLD OF THE OPENCV INRANGE FUNCTION.**

The implication of the threshold value in Figure 8 is explicitly shown for points A, B, C and D in Figure 9. Points A and D show over-detection and under-detection of the perforations for large and small threshold values. Point B shows a miss-detection of the perforation, where the perforation boundary is not fully closed for singular perforations. Point C shows the optimised threshold at the infliction point of the cubic spline regression. The optimised threshold value also correlates best with the visual impression of the perforation.

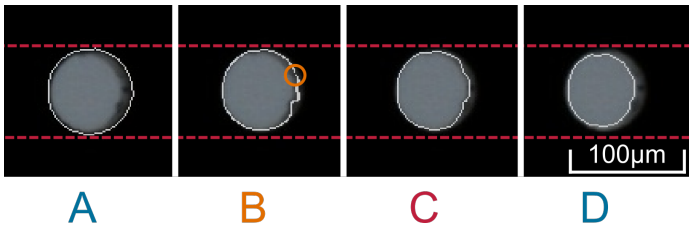


**FIGURE 9: INCREASING THE THRESHOLD REDUCES THE SIZE OF THE DETECTED PERFORATION.**

All detected perforations have unique geometries which cannot be described with one common model. Comparing the different geometry types and the deviation from the intended geometry requires a general geometry description. The authors of this study chose to calculate the centre of area (COA) of each detected perforation and to describe the perforation geometry from its COA by the local radius $r_{local}$ depending on the angle $\omega$. Figure 10 defines an arbitrary perforation geometry's local radius

and angle. The advantage of this general geometry description approach is that the mean perforation geometry of all perforations of one specimen can be determined, including its variations and characteristic parameters such as minimum and maximum radius. Figure 11 shows the mean radius $\bar{r}$, the mean local radius $r_{local}$ and its 95 % confidence interval (CI) of the mean depending on the angle $\omega$ for specimen No. 8. At the same time, this approach allows to compare the average detected perforation geometry to the intended perforation geometry.

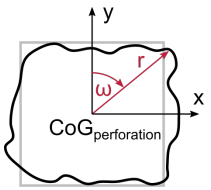


**FIGURE 10: DEFINITION OF THE RADIUS AND ANGLE $\omega$ DEFINING THE EXACT CONTOUR FROM THE CENTRE OF GRAVITY.**

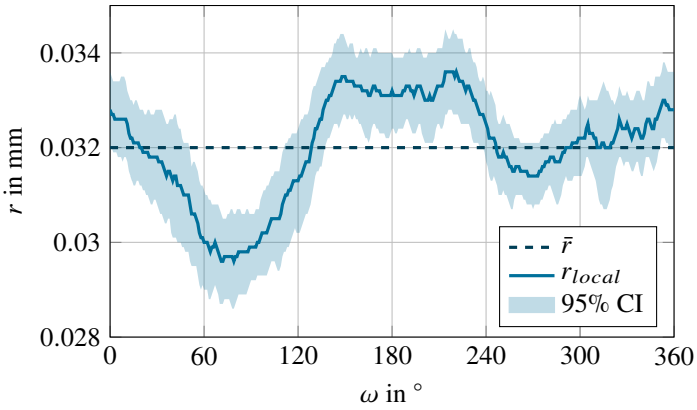


**FIGURE 11: THE VARIATIONS OF THE ETCHED PERFORATIONS OF SPECIMEN 08 WITH A NOMINAL RADIUS OF 0.0315 mm.**

### 2.3 Pressure drop evaluation

The pressure drop measurements of all test specimens were conducted in a flow bench setup at TU Braunschweig's Institute of Fluid Mechanics. The main components of the flow bench are the intake, including the specimen mount, the flowmeter to determine the volume flow and the compressor providing the required vacuum. Figure 12 shows the arrangement of the single components in the flow bench. The pressure taps integrated into the intake are connected to a DTC Initium Pressure Scanning System [29], to measure the pressure on top and below the test specimen. The pressure scanner and the flowmeter are connected to the same data acquisition system for synchronous data recording. For flow rate variations, the compressor power can be manually adjusted. Figure 13 shows the single components of the flow bench.

For the pressure drop measurement, the specimen is mounted in the size reduction adaptor of the flow bench, which is then mounted into the intake section of the flow bench. The volume flow and the pressure at the upper and lower pressure taps are measured at discrete flow rates and logged by the system. The

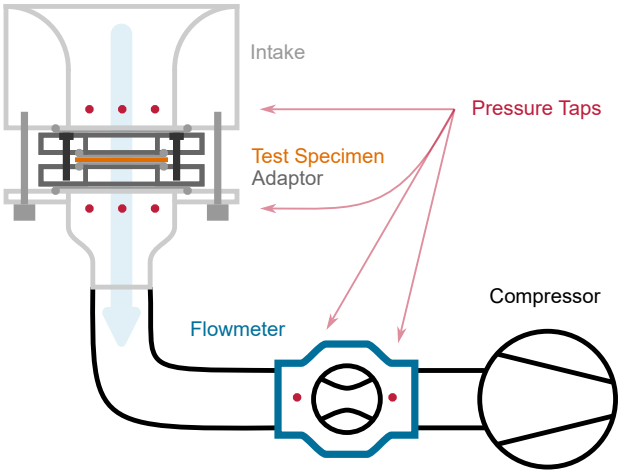


**FIGURE 12: SCHEMATIC FIGURE OF THE FLOW BENCH SETUP FOR PRESSURE DROP EVALUATION.**

exported data contains a time series of pressure and flow data for each discrete flow rate, which can be evaluated as mean differential pressure over the specimen and mean volume flow. If required, the time series also allows the calculation of the uncertainties in the form of standard deviation or confidence interval. An undesirable three-dimensional flow behaviour can be ruled out by comparing the pressure variations between the six upper or lower pressure taps.

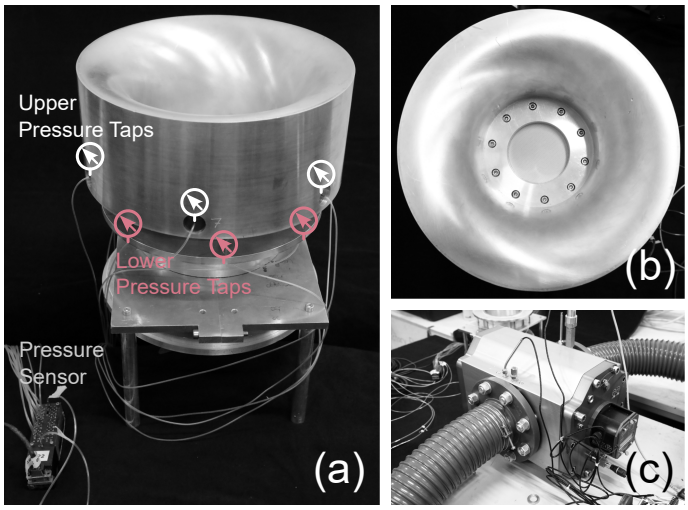


**FIGURE 13: THE FLOW BENCH SETUP FOR THE PRESSURE DROP TESTS OF PERFORATED SKINS: (A) INTAKE; (B) SPECIMEN AND ADAPTER; (C) FLOWMETER.**

### 2.4 Modeling of pressure loss

To investigate pressure loss characteristics through the holes, this study uses the empirical model of Preist and Paluch [15]. In contrast to other models, Preist and Paluch consider the difference between flow-side and plenum-side diameter. This is important, especially for laser-drilled and SLA-printed specimens. Both perforations types designed for the outer cover of an LFC system usually have a smaller equivalent diameter $d$ on the flow side and

a larger equivalent diameter $D$ on the plenum side as shown in Figure 2.

In the Preist model given in Equation (3), the pressure loss through the porous sheet is a function of the average suction velocity $v_o$ normalised by the porosity $\Phi$ resulting in the mean flow velocity in the perforations. Preist et al. modelled the flow through these perforations as a quadratic function with two coefficients $C_a$ and $C_b$ representing the dynamic pressure loss and frictional pressure loss:

$$\Delta p = C_a \left(\frac{v_o}{\phi}\right)^2 + C_b \frac{v_o}{\phi}. \tag{3}$$

Where the coefficients $C_a$ and $C_b$ are defined as:

$$C_a = \frac{C}{2}\rho, \tag{4a}$$

$$C_b = 32K\mu\frac{t}{d^2}, \tag{4b}$$

The constant C, in Equation (4a), is evaluated empirically, and $\rho$ is the air density. In Equation (4b), $K$, the panel thickness $t$ and $d$ are geometrical parameters that describe the hole geometry, and $\mu$ is the viscosity of the air. The diameter variation along the flow direction is accounted for in the frictional loss term using the factor $K$ representing the ratio of smaller and larger diameter $d$ and $D$:

$$K = \frac{1}{4}\frac{d}{D}\left(1 + \frac{d}{D}\right)\left(1 + \left(\frac{d}{D}\right)^2\right). \tag{5}$$

### 2.5 Evaluation of surface roughness

The surface roughness measurements were conducted for each specimen using a laser profilometer. With the profilometer, a representative area of 30 mm by 30 mm was scanned on each specimen in single tracks with a distance of 2 mm and a track resolution of 10 µm. To identify the surface roughness, a Savitzky-Golay filter was applied to remove the global deformation and waviness of the specimen. The filtered data was plotted for the specimens, to get a rough idea of the surface roughness. No further data processing steps were undertaken in the scope of this study since the aim was a rough guess of whether post-processing of AM porous sheets is a necessary prerequisite for LFC.

## 3. RESULTS AND DISCUSSIONS

This paper compares the design and the experimentally obtained perforation parameters for six different porous sheet types. The main perforation parameters are the mean equivalent perforation diameter, the mean pitch and the mean porosity. The mean equivalent diameter thereby describes the perforation size by the diameter of a circular perforation with the same perforation area. The porosity is determined using Equation (1) with the mean pitch and mean equivalent diameter. All parameters are identified using the introduced Python tool and include their 95 % confidence intervals.

Table 2 summarises the specimen's experimentally obtained perforation parameters. While the detected mean pitch of all specimens is generally close to the design pitch and shows a small confidence interval, the equivalent diameter significantly deviates from the design diameter. This results in significant porosity design deviations. The results show that etched SS foils (No. 08-10) exhibit the lowest porosity design deviations resulting from highly accurate mean diameters with small confidence intervals. Specimen No. 08 was measured twice, the second time (No. 08*) with higher image resolution resulting in a porosity design deviation of 0 %. The porosity design deviations of the other etched SS specimens are expected to be reduced to zero by increasing the image resolution. Therefore, all other specimens were investigated with increased image resolution.

In contrast to the etched SS specimens, the laser-drilled specimens (11-13) show larger porosity design deviations, which increase with increasing mean equivalent diameter and its 95 % confidence interval. The SLM specimens (14-18) show the opposite effect where the porosity design deviation increases with decreasing mean equivalent diameter and its 95 % confidence interval. The SLA specimens (19-21) show larger porosity design variations but a smaller 95 % confidence interval at a similar equivalent diameter as the SLM specimens, suggesting higher manufacturing repeatability.

The results show that laser-drilled and SLM-printed porous sheets with nominal diameters of 240 µm and 120 µm can be manufactured with similar size and accuracy. SLA-printed porous sheets can be manufactured so far with rectangular holes of 250 µm by 120 µm at a high repeatability. Etched SS porous sheets show the lowest porosity design deviation at a small nominal diameter of 63 µm, and smaller 95 % confidence interval compared to the laser drilled specimens with similar perforation size. For larger nominal diameters of 200 µm the PC specimen (No. 25) shows the lowest porosity design deviation and smallest 95 % confidence interval. SLM printed specimens with nominal diameters of 60 µm exhibit a mean diameter 95 % confidence interval twice the size of the detected diameter, preventing an even porosity distribution.

The CFRP specimen (No. 07) shows the largest design porosity deviation. Comparisons of the upper and lower hole diameter and micro CT images show that not all needles of the needle bed tooling fully penetrated the specimen, resulting in a significantly smaller diameter caused by the conical shape of the needle. An etched needle bed tooling, where the tool side of the CFRP sheet can later be used as a suction surface, would not require a thick layer of flow aid between the tool and fibre material. Therefore, such a tool is expected to allow full penetration of the CFRP layers. However, since such a tool was unavailable in this study, the CFRP specimen is excluded from further aerodynamic investigations.

The variations of the perforation geometries can be described by the dependency of the local perforation radius on its position on the perforation contour. Figure 14 shows the variations of the local perforation radius $r$ over the angle $\omega$ for all specimens including their 95 % confidence interval. A circular perforation has a constant radius and should be a horizontal line in the plot. In contrast, a square perforation is exemplarily plotted as specimen No. 00. While specimens No. 08, 11 and 25 show an almost constant radius with a narrow 95 % confidence interval,

**TABLE 2: POROSITY RESULTS FOR ALL SPECIMENS.**

| No. | equiv. diameter mean mm | equiv. diameter 95% confidence mm | pitch mean mm | pitch 95% confidence mm | porosity mean % | porosity 95% confidence % | porosity design deviation % |
|---|---|---|---|---|---|---|---|
| 07 | 0.080 | 0.070 - 0.090 | 1.320 | 1.268 - 1.372 | 0.341 | 0.233 - 0.462 | -84 |
| 08 | 0.0614 | 0.0608 - 0.0620 | 0.6270 | 0.6267 - 0.6273 | 0.8691 | 0.8508 - 0.8876 | -4 |
| 08* | 0.0629 | 0.0612 - 0.0646 | 0.6281 | 0.6279 - 0.6284 | 0.9109 | 0.8615 - 0.9590 | 0 |
| 09 | 0.0622 | 0.0616 - 0.0628 | 0.6264 | 0.6261 - 0.6268 | 0.8943 | 0.8772 - 0.9115 | -1 |
| 10 | 0.0602 | 0.0596 - 0.0608 | 0.6236 | 0.6234 - 0.6239 | 0.8447 | 0.8275 - 0.8621 | -7 |
| 11 | 0.0547 | 0.0525 - 0.0570 | 0.5926 | 0.5889 - 0.5964 | 0.7732 | 0.7021 - 0.8487 | -15 |
| 12 | 0.0947 | 0.0898 - 0.0995 | 1.1776 | 1.1750 - 1.1803 | 0.5864 | 0.5253 - 0.6510 | -35 |
| 13 | 0.1688 | 0.1576 - 0.1800 | 2.3485 | 2.3447 - 2.3524 | 0.4685 | 0.4070 - 0.5346 | -48 |
| 14 | 0.236 | 0.229 - 0.242 | 2.4048 | 2.401 - 2.408 | 0.872 | 0.823 - 0.921 | -4 |
| 15 | 0.204 | 0.197 - 0.211 | 2.3984 | 2.393 - 2.404 | 0.654 | 0.607 - 0.702 | -28 |
| 16 | 0.072 | 0.057 - 0.088 | 1.2028 | 1.195 - 1.211 | 0.329 | 0.200 - 0.487 | -64 |
| 17 | 0.087 | 0.079 - 0.096 | 1.2042 | 1.197 - 1.211 | 0.478 | 0.384 - 0.582 | -47 |
| 18 | 0.038 | 0.009 - 0.068 | 0.8012 | 0.782 - 0.820 | 0.208 | 0.010 - 0.687 | -77 |
| 19 | 0.251 | 0.248 - 0.254 | 2.671 | 2.668 - 2.674 | 0.802 | 0.780 - 0.823 | -20 |
| 20 | 0.236 | 0.230 - 0.242 | 2.668 | 2.665 - 2.670 | 0.712 | 0.675 - 0.750 | -29 |
| 21 | 0.293 | 0.290 - 0.296 | 2.671 | 2.670 - 2.673 | 1.089 | 1.065 - 1.113 | 9 |
| 25 | 0.2020 | 0.2004 - 0.2035 | 1.9903 | 1.9889 - 1.9916 | 0.9341 | 0.9185 - 0.9498 | 3 |

all other circular perforated specimens show significant deviations from their design geometry with larger 95 % confidence intervals. SLM printed specimens hereby exhibit the largest deformations. In contrast, the SLA printed specimens (19-21) show a good match with the design geometry (00). However, the edges are slightly rounded, resulting in a reduced peak. As for the equivalent diameter of the SLA specimens, also the 95 % confidence interval of the SLA specimens' radius is narrow suggesting a high repeatability.

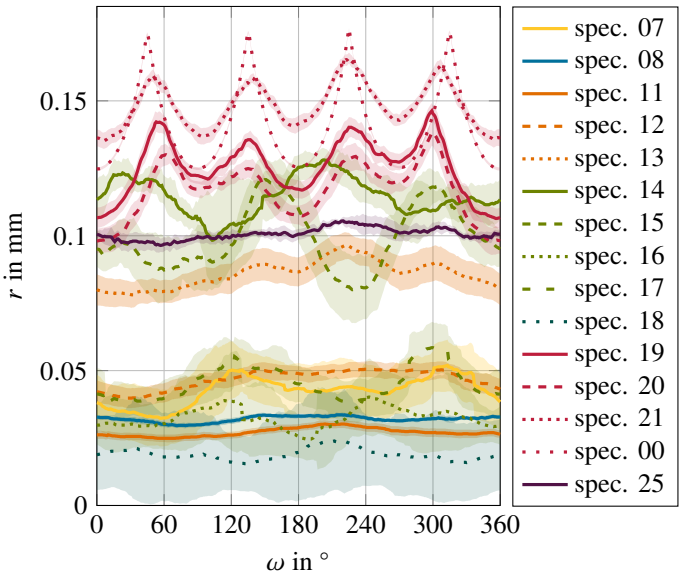


**FIGURE 14: THE MEAN LOCAL RADIUS AND 95% CONFIDENCE INTERVAL FOR ALL SPECIMEN TYPES.**

The surface roughness measurements were conducted exemplary for all specimen types. While etched and laser-drilled specimens show maximum surface roughness heights $\leq 10\,\mu m$, SLA specimens and laser-cleaned SLM specimens show maximum surface roughness heights $\leq 40\,\mu m$ and $\leq 50\,\mu m$. Therefore, post-treatment is also expected to be required for additively manufactured porous sheets.

Figure 15 shows the pressure drop results for all specimens. Some specimens were measured twice to show reproducibility. These measurements are differentiated by solid and open data point markers. The results of the pressure drop measurements indicate a significant dependency of the pressure drop on the porosity, as suggested by the Preist model. Additionally, the curvature decreases with the hole size. This effect is visible for the laser drilled specimens (11-13) and when comparing the etched SS specimens (8-10) featuring small perforations to the SLA printed specimens (19-20) featuring larger perforations. The decreasing curvature can be directly associated with the linear term in the Preist model, which represents the frictional losses.

Equation (3) is fitted to the pressure drop measurements normalised by the measured porosity using a non-linear least square approach to validate the Preist model. Table 3 shows the fitted coefficients $C_{a,fit}$ and $C_{b,fit}$, and the coefficient of determination (R-squared) to measure fit quality. The coefficient of determination close to 1 shows, that the quadratic model is an appropriate model for the pressure drop measurements. However, when comparing the fitted coefficients $C_{b,fit}$ to the coefficients calculated based on the measured perforation size $C_{b,measured}$, only specimens No. 15 and 25 show an acceptable match. While for the etched, laser drilled and SLA-printed specimens, $C_{b,fit}$ and $C_{b,measured}$ show a proportional relationship, no such proportional relationship can be observed for the SLM specimens. Therefore, the Preist model cannot be validated as a universal

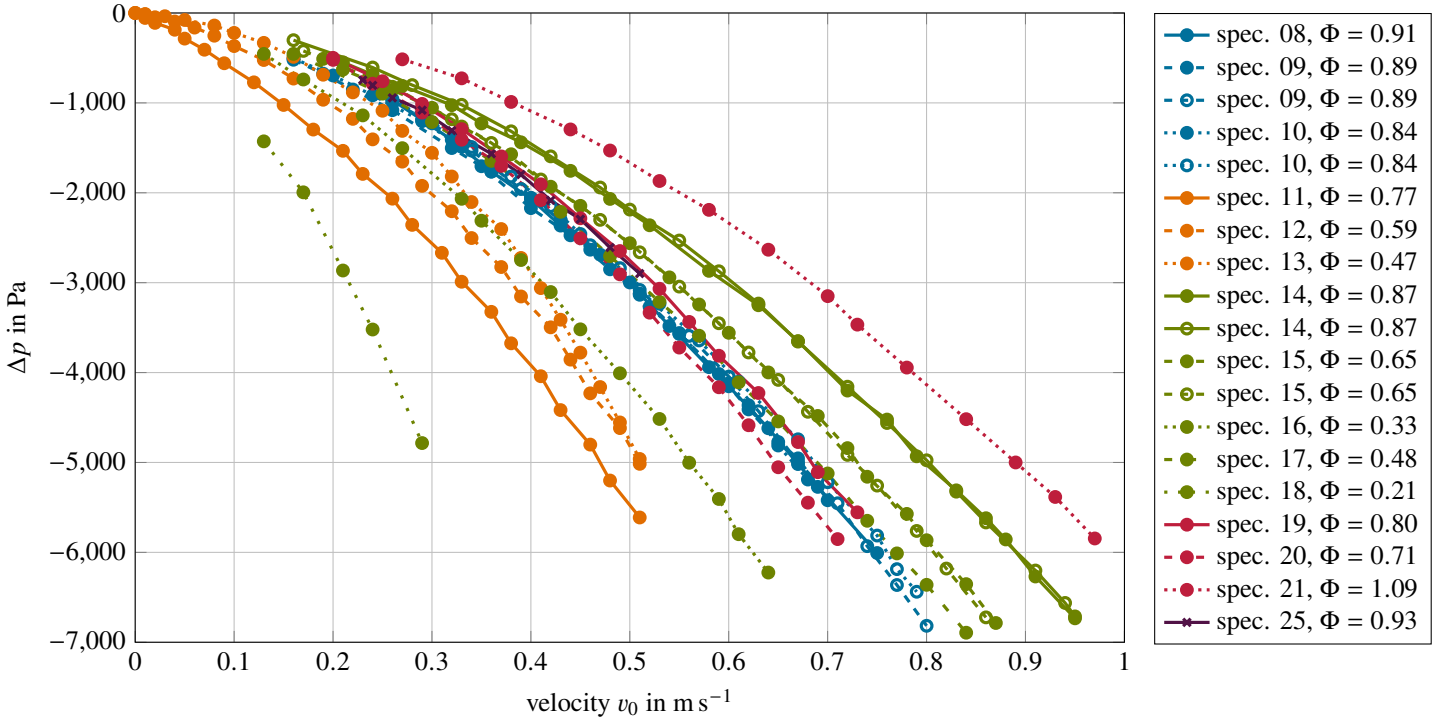


**FIGURE 15: PRESSURE DROP AT THE PERFORATED SKIN DEPENDING ON THE PERFORATION GEOMETRY, POROSITY, AND SUCTION VELOCITY. SOME SPECIMENS WERE TESTED TWICE TO ENSURE REPLICABILITY.**

pressure drop model.

**TABLE 3: FITTED COEFFICIENTS FOR THE PREIST MODEL.**

| No. | $C_{a,fit}$ | $C_{b,fit}$ | $R^2$ | $C_{b,design}$ | $C_{b,measured}$ |
|---|---|---|---|---|---|
| 08 | -0.6997 | -16.4679 | 0.9993 | -7.34 | -7.36 |
| 09 | -0.6667 | -19.0032 | 0.9998 | -7.34 | -7.36 |
| 09* | -0.7190 | -14.4620 | 0.9999 | -7.34 | -7.36 |
| 10 | -0.7259 | -15.1716 | 0.9997 | -7.34 | -7.36 |
| 10* | -0.6770 | -15.5611 | 0.9996 | -7.34 | -7.36 |
| 11 | -0.7174 | -38.5351 | 0.9997 | -129.42 | - |
| 12 | -0.5172 | -12.5688 | 0.9997 | -32.36 | - |
| 13 | -0.4330 | 2.3218 | 0.9988 | -8.09 | - |
| 14 | -0.4572 | -12.2432 | 0.9998 | -8.09 | -8.37 |
| 14* | -0.4730 | -10.5116 | 0.9996 | -8.09 | -8.37 |
| 15 | -0.3127 | -9.6382 | 0.9997 | -8.09 | -11.20 |
| 15* | -0.3226 | -8.9170 | 0.9999 | -8.09 | -11.20 |
| 16 | -0.1221 | -8.5057 | 0.9995 | -32.36 | -89.88 |
| 17 | -0.1731 | -9.3860 | 0.9993 | -32.36 | -61.56 |
| 18 | -0.1584 | -12.2145 | 0.9991 | -129.42 | -322.66 |
| 19 | -0.6112 | -6.1403 | 0.9996 | -0.24 | -0.27 |
| 20 | -0.5458 | -5.0393 | 0.9995 | -0.24 | -0.28 |
| 21 | -0.6943 | -4.3551 | 0.9996 | -0.24 | -0.23 |
| 25 | -0.7482 | -12.1419 | 0.9994 | -11.65 | -11.71 |

## 4. CONCLUSION

This study demonstrates the feasibility of AM and CFRP micro-perforated porous sheets with perforations in the same order of magnitude as available laser-drilled and etched sheets. Although the perforation quality and size of etched SS sheets cannot be reached by additive manufacturing so far, the new porous sheets with new perforation geometries and new manufacturing techniques significantly expand the design space for LFC suction skins. This study has proven that the pressure drop behaviour of high-quality etched foils can be reached with SLA-printed porous sheets featuring quadratic truncated cone perforations. A common model for pressure drop prediction, the Preist model, could not be validated for the new porous sheet types and shows at least questionable results for available etched and laser-drilled sheets.

## ACKNOWLEDGMENTS

This research was funded by the Deutsche Forschungsgemeinschaft (DFG, German Research Foundation) under Germany's Excellence Strategy – EXC 2163/1- Sustainable and Energy Efficient Aviation – Project-ID 390881007.

## REFERENCES

[1] Beck, Nils, Landa, Tim, Seitz, Arne, Boermans, Loek, Liu, Yaolong and Radespiel, Rolf. "Drag Reduction by Laminar Flow Control." *Energies* Vol. 11 No. 1 (2018): p. 252. DOI 10.3390/en11010252.

[2] Krishnan, K.S.G., Bertram, O. and Seibel, O. "Review of hybrid laminar flow control systems." *Progress in Aerospace Sciences* Vol. 93 (2017): pp. 24–52. DOI 10.1016/j.paerosci.2017.05.005.

[3] Joslin, Ronald D. "Aircraft Laminar Flow Control." *Annual Review of Fluid Mechanics* Vol. 30 No. 1 (1998): pp. 1–29. DOI 10.1146/annurev.fluid.30.1.1.

[4] Srinivasan, Kalarikovilagam and Bertram. "Preliminary Design and System Considerations for an Active Hybrid Laminar Flow Control System." *Aerospace* Vol. 6 No. 10 (2019): p. 109. DOI 10.3390/aerospace6100109.

[5] Traub, Hendrik, Wolff, Johannes, Jose, Siby, Lobitz, Lennart, Schollerer, Martin and Hühne, Christian. "Concept and design of extended hybrid laminar flow control suction panels." *Scientific Reports* (2021)DOI 10.21203/rs.3.rs-924184/v1.

[6] Horn, Matthias, Seitz, Arne and Schneider, Marvin. "Novel tailored skin single duct concept for HLFC fin application." *European Conference for Aeronautics and Space Sciences*. 2017. DOI 10.13009/EUCASS2017-44.

[7] Schrauf, Geza and Horstmann, Karl Heinz. "Simplified Hybrid Laminar Flow Control." *European Congress on Computational Methods in Applied Sciences and Engineering*. 2004.

[8] Messaoudia, Hamza, Mehrafsun, Salar, Schrauf, Geza and Vollertsen, Frank. "Highly reproducible laser micro drilling of titanium-based HLFC sections." *Lasers in Manufacturing Conference*. Wissenschaftlichen Gesellschaft Lasertechnik und Photonik e.V. (2015).

[9] Ashkenasi, David, Kaszemeikat, Tristan, Mueller, Norbert, Dietrich, Reinhard, Eichler, Hans Joachim and Illing, Gerd. "Laser Trepanning for Industrial Applications." *Physics Procedia* Vol. 12 (2011): pp. 323–331. DOI 10.1016/j.phpro.2011.03.140.

[10] Young, T. M., Humphreys, B. and Fielding, J. P. "Investigation of hybrid laminar flow control (HLFC) surfaces." *Aircraft design* Vol. 4 No. 2-3 (2001): pp. 127–146.

[11] Lobitz, Lennart, Traub, Hendrik, Overbeck, Mats, Bień, Maximilian, Heimbs, Sebastian, Hühne, Christian, Friedrichs, Jens and Horst, Peter. "Aircraft Wing Design for Extended Hybrid Laminar Flow Control." *Aerospace* Vol. 10 No. 11 (2023): p. 938. DOI 10.3390/aerospace10110938.

[12] CAV Systems. "µLASE - CAV Systems." (2023). Accessed 10.11.2023, URL https://www.cav-systems.com/drag-reduction/%c2%b5lase/.

[13] Poll, D. I.A., Danks, M. and Humphreys, B. E. "The aerodynamic performance of laser drilled sheets." (1992).

[14] Goldstein, Sydney. *Modern developments in fluid dynamics: an account of theory and experiment relating to boundary layers, turbulent motion and wakes*. Clarendon Press (1938).

[15] Preist, J. and Paluch, B. "Design specification and inspection of perforated panels for hlf suction systems." *ONERA* (1996).

[16] Doerffer, Piotr P. and Bohning, Rainer. "Modelling of perforated plate aerodynamics performance." *Aerospace Science and Technology* Vol. 4 No. 8 (2000): pp. 525–534. DOI 10.1016/s1270-9638(00)01063-4.

[17] Gibson, T. M., Babinsky, H. and Squire, L. C. "Passive control of shock wave–boundary-layer interactions." *The Aeronautical Journal* Vol. 104 No. 1033 (2000): pp. 129–140. DOI 10.1017/s000192400002532x.

[18] Wagner, R. D., Maddalon, D. V., Clark, R. L., Chen, A. W., Behbehani, R. and Lund, D. W. "High Reynolds Number Hybrid Laminar Flow Control (HLFC) Flight Experiment II. Aerodynamic Design."

[19] Wagner, R. D., Maddalon, D. V., Clark, R. L., Hamamoto, M., Horstman, R. H. and Cruver, H. A. "High Reynolds Number Hybrid Laminar Flow Control (HLFC) Flight Experiment: IV. Suction System Design and Manufacture."

[20] Schrauf, Geza. *On allowable step heights: lessons learned from the F100 and ATTAS flight tests* (2018). URL https://elib.dlr.de/124546/1/schrauf_2018_ecfd_steps.pdf.

[21] Anderson, G. F., Murthy, V. S. and Sutera, S. P. *Laminar boundary-layer control by combined blowing and suction in the presence of surface roughness (Laminar boundary layer control on two dimensional ...* (1969). URL https://arc.aiaa.org/doi/pdf/10.2514/3.48102.

[22] Prasannakumar, Adarsh, Wolff, Johannes, Radespiel, Rolf, Boermans, Loek, Hühne, Christian and Badrya, Camli. "Design and power calculation of HLFC suction system for a subsonic short-range aircraft." *CEAS Aeronautical Journal* Vol. 13 No. 4 (2022): pp. 1003–1026. DOI 10.1007/s13272-022-00614-1.

[23] Schrauf, Geza H. and von Geyr, Heiko. "Simplified Hybrid Laminar Flow Control for the A320 Fin-Aerodynamic and System Design, First Results." American Institute of Aeronautics and Astronautics (ed.). *AIAA Scitech 2020 Forum*: p. 1536. 2020.

[24] Micrometal. "Wet Chemical Etching of Filters & Sieves | micrometal (Germany)." (2023). Accessed 18.10.2023, URL https://www.micrometal.de/en/products/filters-sieves/#.

[25] photonicfab. "Laserlohnfertiger für die Mikro-Materialbearbeitung - photonicfab." (2023). Accessed 18.10.2023, URL https://photonicfab.de/.

[26] https://www.acupunctureworld.de/. "Acupunctureworld | TeWa 5JB-Type Speed Pack ." (2023). Accessed 19.10.2023, URL https://www.acupunctureworld.de/akupunkturnadeln/starrer-metallgriff/tewa-5jb-type-speed-pack.html.

[27] Carl Zeiss AG. "Smartzoom 5." (07.07.2022). Accessed 07.07.2022, URL https://www.zeiss.com/microscopy/int/products/imaging-systems/smartzoom-5.html.

[28] Bradski, G. "The OpenCV Library." *Dr. Dobb's Journal of Software Tools* (2000).

[29] TE Connectivity. "Dtc Initium Data Acquisition System | DTC Inituim Series." (2023). Accessed 06.11.2023, URL https://www.te.com/usa-en/product-CAT-SCS0010.html.

[30] Hood, R. V., Middleton, D. B. and Hanks, G. W. "Hybrid Laminar Flow Control Study Final Technical Report."

[31] Najmon, Joel C., Raeisi, Sajjad and Tovar, Andres. "Review of additive manufacturing technologies and applications in the aerospace industry." *Additive Manufacturing for the Aerospace Industry*. Elsevier (2019): pp. 7–31. DOI 10.1016/B978-0-12-814062-8.00002-9.

[32] Orfanidis, Sophocles J. *Introduction to signal processing*, 5th ed. Prentice Hall signal processing series, Prentice Hall, Upper Saddle River, N.J. (1996).